Article | Received 14 September 2026; Revised 16 October 2026; Accepted 9 November 2026; Published XX November 2026
https://doi.org/10.55092/bm20260015

Biodegradable PCL/Fe_3O_4/CeO_2 microrobots for magnetically actuated ROS scavenging and osteogenic mineralization

Di Shi[1],†, Yingting Yang[1],† and Jinhua Li[2],*

[1] School of Materials Science and Engineering, School of Interdisciplinary Science, Beijing Institute of Technology, Beijing, China
[2] Beijing Key Laboratory of Digital Diagnosis and Treatment Research and Development for Super-Minimally Invasive Surgery, School of Chemistry and Chemical Engineering, Beijing Institute of Technology, Beijing, China

† These authors contributed equally to this work.

* Correspondence author; E-mail: lijinhua@bit.edu.cn.

Highlights:

- Biodegradable PCL/Fe_3O_4/CeO_2 magnetic microrobots were developed for magnetically actuated navigation and active osteogenic mineralization.
- CeO_2 functionalization provides microrobots with strong ROS-scavenging capacity and cytoprotection against oxidative stress.
- The microrobots significantly promote osteogenic mineralization and degrade gradually under physiological conditions.

Abstract: Repairing bone defects remains a significant clinical challenge because bone tissue has limited self-regenerative capacity. Magnetic micro/nanorobots have emerged as promising platforms for active bone regeneration because they enable targeted delivery and local mechanical stimulation, but their clinical translation is largely hindered by non-degradability and potential oxidative damage from inflammation. We report biodegradable magnetic microrobots composed of polycaprolactone (PCL), iron oxide nanoparticles (Fe_3O_4 NPs), and cerium oxide nanoparticles (CeO_2 NPs) for magnetically actuated navigation and osteogenic mineralization. The PCL/Fe_3O_4/CeO_2 microrobots show a well-defined spherical morphology and superparamagnetic behavior, enabling precise magnetic actuation with an average velocity of 106.85 μm/s. In vitro assays show excellent cytocompatibility, with mesenchymal stem cells adhering and proliferating to fully encapsulate the microrobots by day 7. Benefiting from the strong catalase-mimetic activity of Ce^{4+} species in the incorporated CeO_2 nanoparticles, the microrobots achieve efficient H_2O_2 scavenging performance and effectively protect cells from oxidative stress-induced damage. In addition, incorporating CeO_2 significantly enhances osteogenic differentiation, as shown by a fourfold increase in matrix mineralization compared with pure PCL. Importantly, the microrobots

Copyright©2026 by the authors. Published by ELSP. This work is licensed under Creative Commons Attribution 4.0 International License, which permits unrestricted use, distribution, and reproduction in any medium provided the original work is properly cited.

degrade progressively over 30 days under physiological conditions, matching the early stages of bone healing. Overall, this work presents a biodegradable magnetic microrobot platform that integrates active navigation, ROS scavenging, and osteogenic stimulation, offering a novel strategy for active osteogenic mineralization.

Keywords: microrobots; magnetic control; osteogenic mineralization; biocompatibility

1. Introduction

Repairing bone defects remains a significant challenge in orthopedics and regenerative medicine, particularly for large defects [1], elderly patients [2], or those with systemic diseases [3], where the limited self-repair capacity of bone tissue is often insufficient for effective regeneration [4]. Currently, bone autografts and allografts remain the primary clinical treatments, with autografts considered the gold standard [2,4]. Nevertheless, these conventional approaches are still limited by donor site morbidity, insufficient bioactive signals, and the complex microenvironment of the defect. Although biomaterials and nanomedicine have provided new tools for bone regeneration [5], insufficient vascularization [6], poor retention of therapeutic agents [7], and inadequate local mechanical stimulation [8] continue to limit the effectiveness of minimally invasive treatments. Given these limitations, intelligent therapeutic systems that provide active navigation, prolonged retention, and direct modulation of the regenerative microenvironment are emerging as crucial strategies for bone repair.

Micro/nanorobots (MNRs) are engineered miniature devices that can perform tasks through self-actuated or externally controlled propulsion [9–11], and they are increasingly regarded as tools for precision and minimally invasive biomedicine [12–14]. Their small size and deep-tissue penetration distinguish them from conventional therapeutic platforms and enable applications in environmental remediation [15,16], targeted delivery [10,12], biosensing [17,18], and minimally invasive surgery [19,20]. For instance, self-propelled MNRs treat rheumatoid arthritis by modulating immune responses and scavenging reactive oxygen species (ROS), with propulsion driven by the decomposition of hydrogen peroxide (H_2O_2) in the inflammatory microenvironment [21]. However, the complex and confined *in vivo* environments place strict demands on MNR penetration and controllability. Compared with other propulsion methods, magnetic propulsion is fuel-free [12], reconfigurable [22], programmable [23], and offers strong tissue penetration [24], enabling magnetically driven MNRs to traverse deep tissues safely with negligible attenuation *in vivo* [25,26]. Magnetic MNRs can promote bone formation through localized micromotion [4,27], deliver therapeutics to treat local inflammation [28,29], and transport stem cells to support bone repair [30] and regeneration [31–33].

Despite this promise, the translation of magnetic MNRs remains limited by biosafety and biodegradability concerns, particularly regarding the long-term fate of residual magnetic components after task completion [34,35]. Compared with cobalt and nickel, iron oxide nanoparticles (Fe_3O_4 NPs) exhibit superior biocompatibility [36]. Therefore, incorporating iron oxide NPs offers advantages over magnetic surface coatings. Moreover, magnetic materials may also generate reactive oxygen species (ROS) through Fenton/Fenton-like reactions [37], thereby potentially causing tissue damage that could compromise regeneration. Cerium oxide (CeO_2) NPs have recently emerged as bioactive nanomaterials for bone tissue engineering [38,39]. Moreover, they exhibit superoxide dismutase and catalase-mimetic activities, which scavenge ROS and protect cells from oxidative stress [40–42]. In addition, CeO_2 NPs can upregulate

osteogenic gene expression and promote mineralization, thus facilitating bone formation [43,44]. However, the therapeutic efficacy of CeO_2 nanoparticles as standalone agents in bone defect repair is limited [38,45]. To address this issue, loading CeO_2 onto magnetically controlled microrobots enables combining active transport and targeted delivery with the ROS scavenging and osteoinductive properties of nanoceria.

The research aim of this work is to develop biodegradable magnetic microrobots composed of polycaprolactone (PCL), Fe_3O_4 NPs, and CeO_2 NPs for magnetically controlled navigation and osteogenic mineralization. Under external magnetic fields, the microrobots moved quickly in straight lines at 106.85 μm/s and showed superparamagnetic behavior with enough magnetization for precise control. In vitro cell experiments showed excellent cytocompatibility, as bone marrow mesenchymal stem cells adhered to and proliferated on the microrobot surface over time. The addition of CeO_2 gave the microrobots strong ROS- scavenging ability, as shown by the efficient breakdown of H_2O_2 and significant protection of cells against oxidative stress. Furthermore, the magnetic microrobots significantly enhanced osteogenic differentiation, indicated by a strong increase in matrix mineralization. Importantly, the microrobots degraded gradually over 30 days under physiological conditions, slowly losing their spherical shape. Collectively, this work presents a biodegradable magnetic microrobot that integrates navigation, cytoprotection, and osteogenic stimulation, providing a novel and promising platform for active bone repair.

2. Methods

2.1. Materials

Polycaprolactone (PCL, Mw = 70,000–90,000) was purchased from Sigma-Aldrich (USA). Fe_3O_4 nanoparticles (20 nm) and CeO_2 nanoparticles (10 nm) were obtained from Aladdin Reagent Co., Ltd. (China). Polyvinyl alcohol (PVA, 87%–89% hydrolyzed, Mw = 31,000–50,000) was supplied by Macklin Biochemical Co., Ltd. (China). Dichloromethane (DCM) and other analytical-grade reagents were purchased from Sinopharm Chemical Reagent Co., Ltd. (China).

Fetal bovine serum (FBS), α-minimum essential medium (α-MEM), penicillin-streptomycin solution, and trypsin-EDTA were purchased from Gibco (USA). Cell Counting Kit-8 (CCK-8), Calcein-AM staining kit, and Alizarin Red S (ARS) were obtained from Beyotime Biotechnology (China). Hydrogen peroxide (H_2O_2, 30%), dissolved oxygen detection reagents, β-glycerophosphate, ascorbic acid, and dexamethasone were provided by Sigma-Aldrich (USA). Rat bone marrow mesenchymal stem cells (rBMSCs) were purchased from Cyagen Biosciences (China).

2.2. Fabrication of PCL/Fe_3O_4/CeO_2 microrobots

A dispersion of PCL mixed with Fe_3O_4 magnetic nanoparticles was prepared at room temperature. Specifically, 350 mg of PCL was dissolved in 4 mL of DCM, followed by the addition of 8 mg of Fe_3O_4 magnetic nanoparticles and 25 mg of Span 80. The mixture was thoroughly vortexed to obtain a PCL/Fe_3O_4 magnetic nanoparticle dispersion.

2 g of PVA was dissolved in 40 mL of distilled water to prepare a PVA solution. Then, 4 mL of the PCL/Fe_3O_4 magnetic nanoparticle dispersion was added dropwise into 2 mL of the PVA solution, and

the mixed solution was emulsified by ultrasonication in an ice-water bath for 2 min to obtain a PCL/Fe_3O_4 magnetic nanoparticle emulsion.

The inner and outer needle channels of a coaxial needle were connected to two separate syringes. The PCL/Fe_3O_4 magnetic nanoparticle emulsion was rapidly injected into the syringe connected to the inner needle of the coaxial needle, which had an inner needle diameter of 0.3 mm, while the PVA solution was loaded into the syringe connected to the outer needle, which had an outer needle diameter of 0.92 mm. The two syringes were fixed and connected to an external dispensing machine. The extrusion pressure for printing through the inner needle was set to 5 kPa, and that for the outer needle was set to 10 kPa. Coaxial printing was performed with simultaneous extrusion to fabricate magnetic microparticles. The printed magnetic microparticles were immediately transferred into the PVA solution and stirred overnight using a mechanical stirring apparatus, with the stirring temperature controlled at 20–25 °C and the stirring speed at 320 rpm.

Subsequently, 10 mg of PEI was dissolved in 50 mL of distilled water, and 320 mg of the magnetic microparticles were added and dispersed by mechanical stirring. PEI was coated onto the surface of the magnetic microparticles via electrostatic adsorption. After stirring for 4 h, 16 mg of CeO_2 particles were added, and stirring was continued overnight to immobilize CeO_2 on the surface of the magnetic microparticles, which produced magnetically controllable bone-repair microrobots.

2.3. Materials characterization

For microstructural characterization, scanning electron microscopy (SEM) was employed to observe the surface morphology of the microrobots (Zeiss Supra 55, Germany). Elemental mapping was analyzed by energy-dispersive X-ray spectroscopy (EDS) equipped with the SEM system. X-ray diffraction (XRD) measurements were conducted to characterize the crystal structures of samples (Rigaku D/MAX-2550 diffractometer, Japan) with Cu Kα radiation in the 2θ range of 5°–90°. X-ray photoelectron spectroscopy (XPS) analysis was performed (Axis Supra + spectrometer, Japan) with monochromatized Al Kα radiation (hν = 1486.8 eV) as the excitation source. The chemical compositions of the samples were analyzed based on adsorption spectra obtained using Fourier transform infrared spectroscopy (FTIR) (Bruker Tensor 27, Germany) in the wavenumber range of 400–4000 cm^{-1}. Zeta potential measurements were carried out in deionized water (Microtrac Nanotrac wave II, USA). The magnetic properties were measured by a vibrating sample magnetometer (VSM, Lake Shore 7404, USA) at room temperature with a magnetic field range of −1.0 T to 1.0 T. The motion performance of microrobots was evaluated by capturing and analyzing their motion movies using an inverted fluorescence microscope (Nikon Eclipse Ts2, Japan). The motion speed was calculated by tracking the displacement of microrobots within a fixed time interval.

2.4. Cellular toxicity and viability

The rBMSCs were cultured in α-MEM supplemented with 10% FBS and 1% penicillin-streptomycin at 37 °C in a 5% CO_2 humidified atmosphere. Before cell viability assessment, microrobot samples were sterilized with 75% ethanol and UV irradiation. rBMSCs were seeded in 24-well plates at a density of 1×10^4 cells per well and co-cultured with microrobots for 1, 3, and 7 days. According to the manufacturer's instructions for the CCK-8 kit, the optical density (OD) at 450 nm was measured on days

1, 3, and 7 (n = 3) using a microplate reader (BioTek Synergy H1, USA). Cell viability was evaluated on days 1, 3, and 7 after seeding using a Calcein-AM staining kit and observed with a fluorescence microscope (Nikon TI-E, Japan).

2.5. Alizarin red staining

The rBMSCs were seeded in 12-well plates at a density of 2×10^4 cells per well. After 24 h of incubation, the initial medium was replaced with osteoinductive medium (α-MEM containing 10% FBS, 10 mM β-glycerophosphate, 50 μg/mL ascorbic acid, and 100 nM dexamethasone) and replenished every 3 days to promote osteogenic differentiation. The rate of osteogenic differentiation was evaluated using alizarin red staining. At the end of the 14-day treatment period, the cells were thoroughly washed with PBS and fixed with 4 % paraformaldehyde (PFA) for 15 min, followed by staining with 2 % alizarin red S (pH 4.1–4.3) for 20 min. Excess stain was gently washed off with PBS to preserve the integrity of the stained mineral deposits. Images of the stained samples were captured using an optical microscope. For semi-quantitative analysis, the stained calcium deposits were dissolved in 10% cetylpyridinium chloride solution, and the absorbance at 405 nm was measured.

2.6. In vitro degradation test

The *in vitro* degradation behavior was assessed by immersing the microrobots in phosphate-buffered saline (PBS, pH 7.4) at 37 °C under constant shaking. At predetermined time points (0, 1, 3, 7, 14, and 30 days), samples were collected and examined under an optical microscope to document morphological changes during degradation.

2.7. Antioxidant activity evaluation

The H_2O_2 decomposition capacity of microrobots was evaluated using a colorimetric titanium sulfate assay kit. Briefly, 10 mg of samples were added to 10 mL of 10 mM H_2O_2 solution. The dissolved oxygen concentration was recorded every 5 min for 60 min using a dissolved oxygen meter. Pure H_2O_2 solution and PCL microspheres were set as controls. After 60 min of reaction, the residual H_2O_2 concentration was determined by a titanium sulfate colorimetric method. The absorbance at 405 nm was measured (n = 3), and the residual H_2O_2 concentration was calculated according to the standard curve.

For antioxidant properties of the microrobot *in vitro*, rBMSCs were seeded in 96-well plates at 5×10^3 cells per well. After 24 h incubation, the medium was replaced with medium containing serial concentrations of H_2O_2 with or without microrobot pretreatment. After 24 h treatment, cell viability was measured by the CCK-8 assay (n = 3). Cells without H_2O_2 treatment served as the control.

2.8. Statistical analysis

Each experiment was performed in triplicate unless otherwise specified. The data are presented as the mean ± SD. Statistical analysis consisted of using an unpaired Student's t-test to evaluate the differences between the groups, and values of $^*p < 0.05$, $^{**}p < 0.01$, $^{***}p < 0.001$, and $^{****}p < 0.0001$ were considered statistically significant.

3. Results

3.1. Fabrication and physicochemical characterization of microrobots

The PCL/Fe_3O_4/CeO_2 microrobots were fabricated by a double emulsion solvent evaporation method. The morphology and elemental distribution of the PCL/Fe_3O_4/CeO_2 microrobots were characterized by scanning electron microscopy (SEM) and EDS mapping, as shown in Figure 1. The low-magnification SEM image showed that the prepared microrobots had a regular spherical shape with good monodispersity, with an average particle size of 240–360 μm. The high-magnification image revealed a rough and granular surface texture, which was attributed to the embedded inorganic nanoparticles on the surface of the PCL matrix. This rough surface is expected to facilitate cell adhesion and extracellular matrix deposition during bone regeneration. EDS elemental mapping (Figure 1b) demonstrated the presence and distribution of Fe and Ce on the microrobot surface. Both Fe (corresponding to Fe_3O_4) and Ce (corresponding to CeO_2) were distributed throughout the microsphere, confirming the co-loading of magnetic and bioactive nanoparticles. These results confirmed the fabrication of ternary composite microrobots with the designed structure.

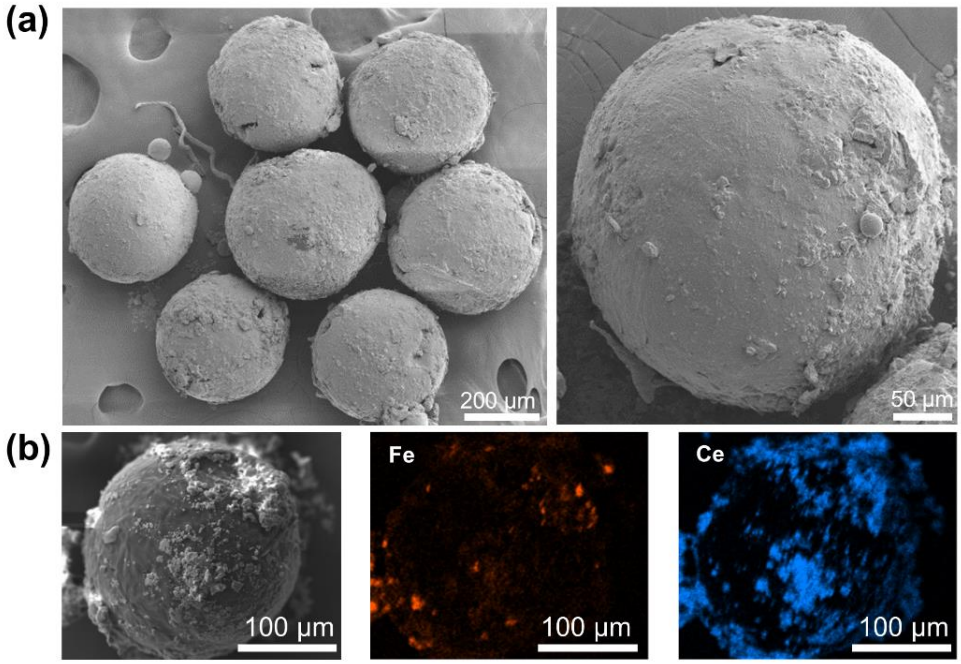


Figure 1. Morphology of PCL/Fe_3O_4/CeO_2 microrobots. **(a)** SEM images of swarms (left) and an individual (right) PCL/Fe_3O_4/CeO_2 microrobot; **(b)** EDS mapping of a PCL/Fe_3O_4/CeO_2 microrobot with iron and cerium on its surface.

To further confirm the crystal phase, chemical composition, and surface properties of the composite microrobots, XRD, XPS, zeta potential analysis, and FTIR were performed (Figure 2). The XRD patterns showed that the characteristic diffraction peaks of Fe_3O_4 (PDF#75-0449) and CeO_2 (PDF#75-0076) were present in the composite microrobots, while the characteristic peaks of PCL (21.4° and 23.7°) were well preserved, indicating that the incorporation of inorganic nanoparticles did not disrupt the crystalline structure of the PCL matrix. The lower peak intensity of PCL in the composite was due to dilution by the inorganic nanoparticles, which also indicated that nanoparticle incorporation partly limited PCL

crystallization. The XPS full spectrum (Figure S1) showed clear peaks of C 1s, O 1s, Fe 2p, and Ce 3d, confirming the coexistence of the PCL matrix, Fe_3O_4, and CeO_2 on the microrobot surface. The fine XPS spectrum of Ce 3d (Figure 2b) confirms that cerium in the as-fabricated microrobots exists primarily in the Ce^{4+} valence state, which serves as the core chemical basis for the prominent catalase-like ROS scavenging performance and enhanced osteogenic bioactivity of the CeO_2 component. This result was consistent with the EDS analysis and provided complementary evidence for the surface chemical composition based on electronic structure.

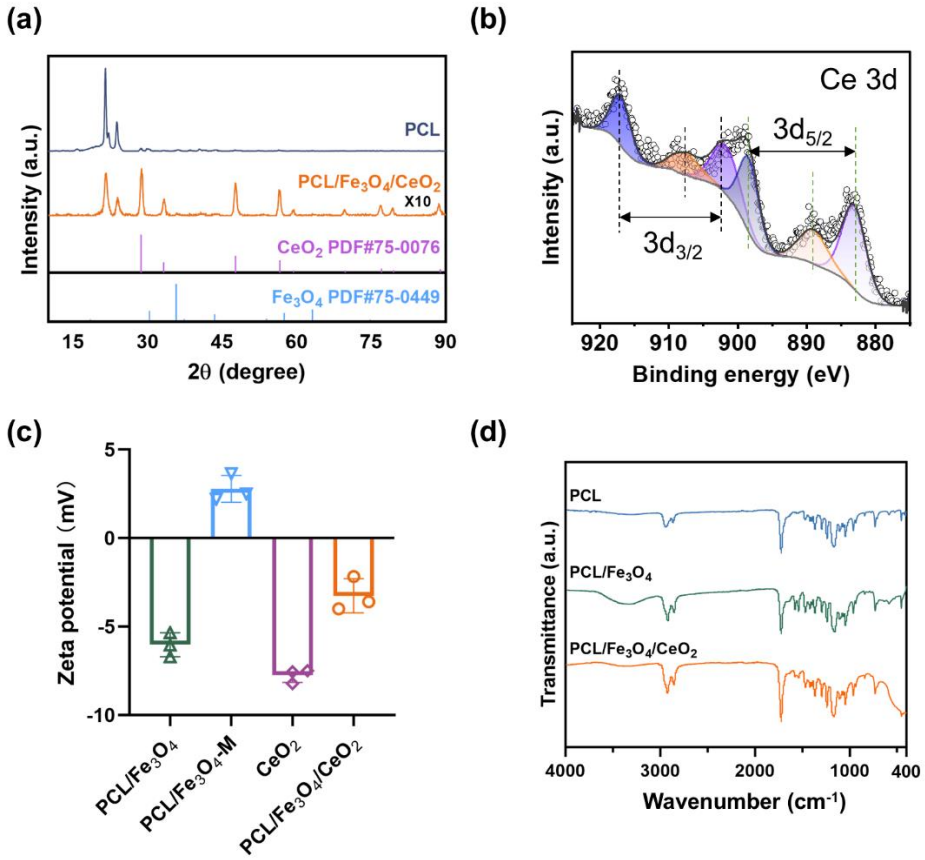


Figure 2. Chemical structure and surface property characterization of PCL/Fe_3O_4/CeO_2 microrobots. **(a)** XRD patterns of pure PCL, PCL/Fe_3O_4/CeO_2 composite, and standard reference cards for Fe_3O_4 (PDF#75-0449) and CeO_2 (PDF#75-0076); **(b)** Fine XPS spectrum of Ce 3d; **(c)** Zeta potentials of PCL/Fe_3O_4, PCL/Fe_3O_4-M (PEI was electrostatically adsorbed onto the PCL/Fe_3O_4, thereby rendering the surface positively charged), CeO_2, and PCL/Fe_3O_4/CeO_2 samples; **(d)** FTIR spectra of pure PCL, PCL/Fe_3O_4, and PCL/Fe_3O_4/CeO_2 microrobots.

Furthermore, zeta potential measurements were performed to investigate surface charge changes during stepwise assembly (Figure 2c). PCL/Fe_3O_4 microrobots had a zeta potential of approximately −6 mV. After surface modification, the potential became positive (approximately +3 mV), which facilitated the subsequent loading of negatively charged CeO_2 nanoparticles through electrostatic interaction. The final PCL/Fe_3O_4/CeO_2 microrobots had a weakly negative potential (approximately –4 mV), which is favorable for serum protein adsorption and cell adhesion in physiological environments. FTIR spectra (Figure 2d) confirmed the chemical structure of each component. Pure PCL showed characteristic absorption peaks at 2940 cm^{-1} and 2860 cm^{-1} (C-H stretching), 1720 cm^{-1} (ester C=O stretching), and 1000–1200 cm^{-1} (C-O-C stretching). All these peaks remained in the composite

microrobots, indicating that the main chain structure of PCL was not destroyed during fabrication. After adding Fe_3O_4 and CeO_2, the absorption peaks in the low wavenumber region (500–600 cm^{-1}) corresponding to metal-oxygen (Fe-O, Ce-O) bonds gradually increased. No new characteristic peaks appeared, suggesting that the components were mainly combined through physical interactions and weak intermolecular forces such as hydrogen bonds.

3.2. Magnetic properties and magnetically actuated navigation

Magnetic responsiveness is the key property that enables active motion in microrobots. The magnetic properties and motion behavior of the microrobots were systematically evaluated, as shown in Figure 3. The magnetic hysteresis loops measured using a vibrating sample magnetometer (VSM) (Figure 3b) showed that both PCL/Fe_3O_4 and PCL/Fe_3O_4/CeO_2 microrobots exhibited typical superparamagnetic behavior: negligible coercivity and remanence, and rapid magnetization in response to an external magnetic field. This superparamagnetic behavior is important for *in vivo* applications, as it prevents irreversible aggregation after removal of the magnetic field, thus reducing the risk of vascular embolism. The saturation magnetization (Ms) values of PCL/Fe_3O_4 and PCL/Fe_3O_4/CeO_2 microrobots were approximately 0.65 and 0.55 emu/g, respectively. The slight decrease in Ms relative to PCL/Fe_3O_4 microrobots is attributed to the non-magnetic nature of CeO_2. This magnetization level was sufficient to drive the directional movement of microrobots in physiological fluids.

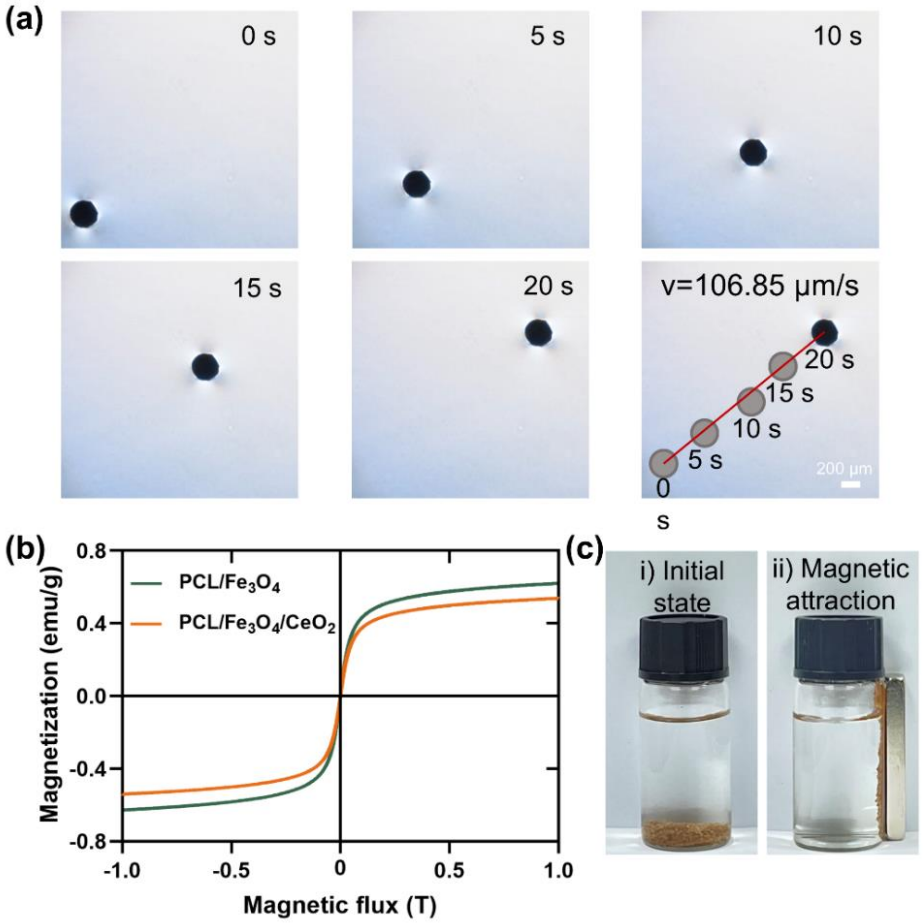


Figure 3. Magnetic actuation performance of the microrobots. **(a)** Microrobot moving under a magnetic field; **(b)** Magnetic hysteresis curves of PCL/Fe_3O_4 and PCL/Fe_3O_4/CeO_2 microrobots measured by VSM; **(c)** Photographs showing responses of microrobots to magnetic attraction.

As shown in Figure 3a, the motion of a single microrobot under an external magnetic field was recorded by optical microscopy. The microrobot moved along a straight path at a stable velocity driven by a magnetic field gradient. The average speed was 106.85 μm/s, comparable to that of other magnetic polymer microrobots, meeting the requirements for local navigation in bone defect sites. Video S1 and Video S2 showed the individual and collective motion of PCL/Fe_3O_4/CeO_2 microrobots. Furthermore, the microrobot maintained structural integrity during movement without fragmentation, demonstrating good mechanical stability. The macroscopic magnetic response was also verified by the magnetic attraction test (Figure 3c). Initially, the microrobots settled at the bottom of the vial, then quickly migrated and aggregated on the side near the magnet within seconds, leaving the solution clear. These results demonstrate the magnetic navigation capability and controllability of the microrobots.

3.3. In vitro cytocompatibility and osteogenesis

To evaluate the intrinsic osteogenic activity of the microrobots, osteogenic induction was performed without applying an external magnetic field. The viability and adhesion behavior of rBMSCs on different microrobot samples were evaluated. As shown in Figure 4, the CCK-8 assay results showed that all groups maintained cell viability above 90% after 7 days of co-culture, and no significant cytotoxicity was observed even at the highest microrobot concentration of 25 mg/mL. As culture time increased, cell viability in all groups increased steadily, indicating that the microrobots supported continuous cell proliferation. Cells cultured with microrobots containing CeO_2 showed slightly higher viability than those cultured with pure PCL microrobots on day 7, which may be related to the antioxidant activity of CeO_2 that improved the cell survival microenvironment.

To further assess cell-material interactions, Calcein-AM fluorescence staining provided a direct view of cell adhesion and growth on the microrobot surface (Figure 4b). Cells cultured on the plate bottom (control group) proliferated rapidly and reached near-confluence on day 7. For cells grown on the three-dimensional spherical surface of the microrobots, only a few adherent cells were observed on day 1. The number of adherent cells increased markedly on day 3, and cells gradually spread along the curved surface. By day 7, a continuous cell layer had formed on the microrobot surface. Moreover, Video 3 showed fluorescence images of cell-loaded PCL/Fe_3O_4/CeO_2 microrobots in motion, further demonstrating their excellent cytocompatibility. These results showed that the PCL/Fe_3O_4/CeO_2 microrobots had good cytocompatibility and could support cell adhesion, spreading, and proliferation, providing a cellular basis for subsequent bone regeneration.

Biodegradability is a key advantage of this microrobot system over traditional non-degradable magnetic microrobots. The morphological changes of the microrobots during degradation in PBS were monitored by optical microscopy (Figure S2). At day 0, the microrobots had an intact spherical shape with smooth edges and a dense structure. At the early stage of degradation (days 1–3), the overall spherical shape was largely maintained, but the surface became slightly rough, and small degradation fragments appeared around the microrobots, indicating that degradation started from the surface through hydrolysis. From day 7, the microrobots showed clear structural deformation and collapse, with sunken and broken spherical contours, suggesting that hydrolysis had penetrated the interior of the matrix. As degradation continued (days 14–30), the integrity of the microspheres was further disrupted, and most of them broke into irregular fragments. By day 30, the original spherical structure had almost completely collapsed, leaving only fragmented aggregates. In addition, the Ce^{4+} concentration in the degradation

medium remained at an extremely low level (0.6–1.13 ppb) throughout the 30 days, with no time-dependent increase (Table S1). This indicates that the CeO_2 nanoparticles were stably retained within the PCL matrix and did not undergo appreciable dissolution, suggesting that the observed morphological changes mainly originated from hydrolysis of the PCL matrix.

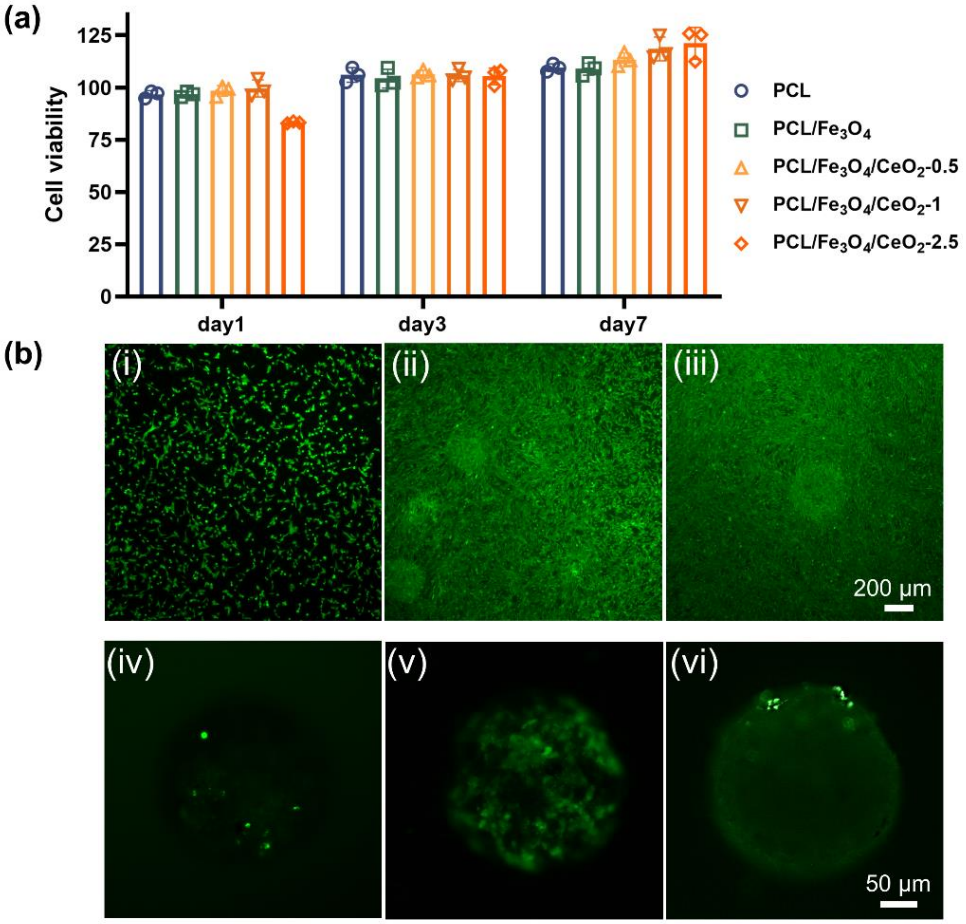


Figure 4. *In vitro* cytocompatibility of PCL/Fe_3O_4/CeO_2 microrobots with rBMSCs. **(a)** Evaluation of proliferation characteristics of cells cultured on PCL microspheres, PCL microspheres@Fe_3O_4 NPs, and microrobots containing CeO_2 NPs at different concentrations (The concentrations represented by PCL/Fe_3O_4/CeO_2-0.5, -1, and -2.5 are 5 mg/mL, 10 mg/mL, and 25 mg/mL, respectively) for 1, 3, and 7 days (n = 3); (**b**) Representative fluorescent staining images of cells cultured on the plate bottom (i, iii, v) and on the surface of the PCL/Fe_3O_4/CeO_2 microrobot (ii, iv, vi) at days 1, 3, and 7 post-seeding.

After 14 days of osteogenic induction, the osteogenic activity of the microrobots was evaluated by ARS staining, a hallmark of late-stage osteogenic differentiation. As shown in Figure 5, qualitative staining images showed that the PCL/Fe_3O_4/CeO_2 group had the densest and most intense red staining, indicating the highest level of calcium deposition and mineralized nodule formation. The PCL/Fe_3O_4 group showed moderate mineralization, whereas the pure PCL group showed minimal mineralization with scattered mineralized nodules. Quantitative analysis was performed by dissolving the stained calcium nodules and measuring the optical density at 405 nm, which further confirmed this trend (Figure 5, right panel). The OD value of the PCL/Fe_3O_4/CeO_2 group was approximately 4-fold higher than those of the pure PCL group ($p < 0.0001$) and the PCL/Fe_3O_4 group ($p < 0.001$). These results

showed that incorporating CeO_2 nanoparticles significantly enhanced the osteogenic potential of the microrobots, providing a strong basis for active bone repair.

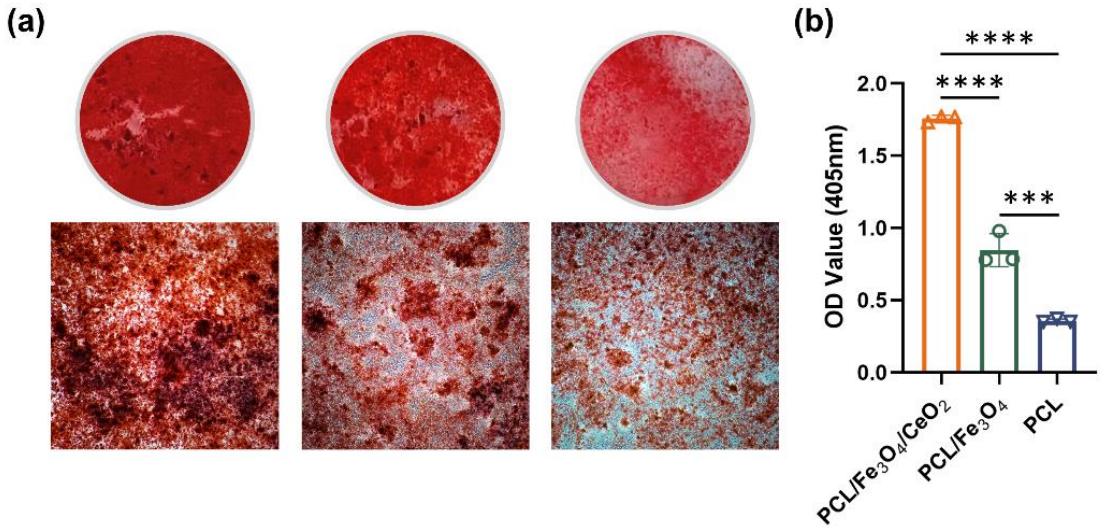


Figure 5. Regulation of osteogenic differentiation of rBMSCs. **(a)** Visualization of mineralized matrix formation by ARS staining after 14 days of co-culture; **(b)** Quantitative analysis of ARS staining. All data are presented as mean ± SD (n = 3; *P < 0.05, **P < 0.01, ***P < 0.001 and ****P < 0.0001).

3.4. Antioxidant and ROS-scavenging capabilities

Oxidative stress caused by excessive ROS at bone defect sites is a major factor that impedes bone regeneration. The antioxidant capacity and cytoprotective effect of the microrobots were investigated. Figure 6a shows the H_2O_2 decomposition kinetics, in which the dissolved oxygen concentration in the PCL/Fe_3O_4/CeO_2 group increased rapidly and linearly with time, reaching 11.4 mg/L at 60 min, indicating strong catalytic activity toward H_2O_2. In contrast, the PCL/Fe_3O_4 group showed only a slow increase in dissolved oxygen, while the pure PCL group and the H_2O_2 control group remained almost unchanged. The residual H_2O_2 concentration at the reaction endpoint (Figure 6b) confirmed this result: the residual H_2O_2 in the PCL/Fe_3O_4/CeO_2 group was the lowest (~3.0 mM), significantly lower than that of the PCL/Fe_3O_4 group (~5.8 mM) or the pure PCL group (~8.8 mM) ($p < 0.0001$).

The strong ROS-scavenging ability of CeO_2 originates from the Ce^{4+} species incorporated on the nanoparticle surface, which mimics superoxide dismutase and catalase and can continuously scavenge ROS without being consumed. This property is important for bone repair, as it can mitigate the inflammatory oxidative microenvironment at the defect site. An H_2O_2-induced oxidative damage cell model was further established to verify the cytoprotective effect. As H_2O_2 concentration increased, cell viability decreased in a dose-dependent manner and was only about 10% at 1.28 mM H_2O_2, indicating that the oxidative damage model was successfully established (Figure 6c). When co-cultured with the microrobots (Figure 6d), cell viability improved significantly at the same H_2O_2 concentration. In particular, at 1.28 mM H_2O_2, the cell viability of the PCL/Fe_3O_4/CeO_2 group remained above 55%, much higher than that of the damage control group. These results show that the microrobots can protect cells from oxidative stress injury by scavenging ROS, an important mechanism for promoting bone regeneration.

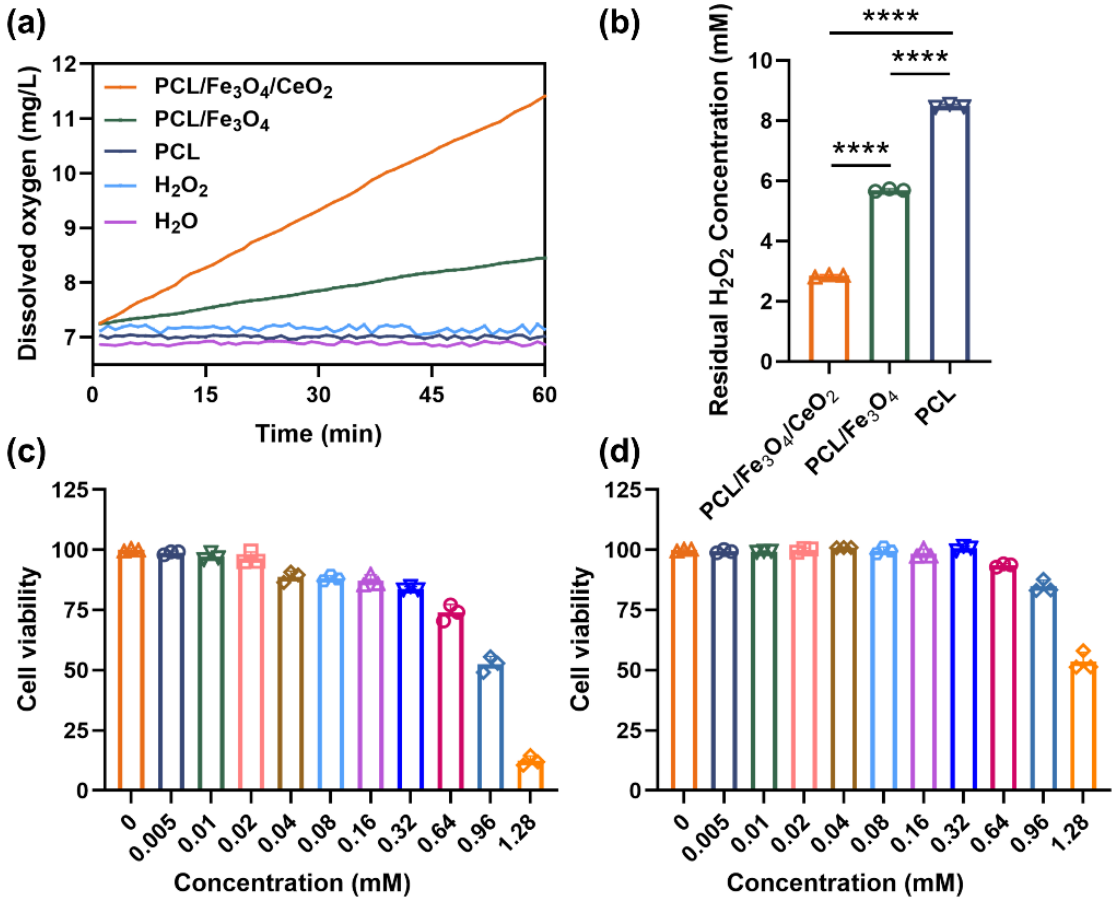


Figure 6. $PCL/Fe_3O_4/CeO_2$ microrobots exhibit antioxidant effects. **(a)** The curve of dissolved oxygen ($PCL/Fe_3O_4/CeO_2$, PCL/Fe_3O_4, PCL, H_2O_2, and H_2O); **(b)** Analysis of the residual H_2O_2 concentration; **(c, d)** Analysis of cell viability with or without microrobot pretreatment. All data are presented as mean ± SD (n = 3; *P < 0.05, **P < 0.01 and ***P < 0.001).

4. Discussion

The ideal bone repair strategy should not only provide structural support but also actively modulate the regenerative microenvironment. In this study, we developed biodegradable magnetic microrobots that integrate multiple therapeutic functions. Their superparamagnetic behavior ensures safe operation *in vivo* by preventing aggregation after removal of the magnetic field, while allowing precise navigation under external magnetic guidance. The rough surface topography and excellent cytocompatibility support cell adhesion and proliferation, providing a favorable interface for tissue integration.

A key feature of this work is the incorporation of CeO_2 NPs, which have two functions: ROS scavenging and osteogenic stimulation. Bone defects have an inflammatory microenvironment with high ROS levels, which can inhibit osteogenic differentiation and promote osteoclastogenesis. Our results show that the CeO_2-incorporated microrobots effectively scavenge H_2O_2 and protect rBMSCs from oxidative stress-induced damage. This cytoprotective effect, together with the osteogenic effects of CeO_2, results in significantly enhanced matrix mineralization. In addition, the degradation profile of the PCL matrix matches the timeline of early bone healing, so the microrobots provide temporary support without long-term residue concerns.

5. Conclusion

In this work, we prepared biodegradable PCL/Fe_3O_4/CeO_2 magnetic microrobots for active osteogenic mineralization by a simple emulsion solvent evaporation method. The microrobots had a uniform spherical shape and a homogeneous distribution of functional components. Chemical characterization confirmed the successful integration of the PCL matrix, Fe_3O_4 magnetic nanoparticles, and CeO_2 bioactive nanoparticles. The microrobots showed superparamagnetic behavior and could move directionally at 106.85 μm/s under an external magnetic field, enabling precise active navigation. In vitro biological experiments showed that the microrobots had excellent cytocompatibility and supported cell adhesion and proliferation. Benefiting from the strong catalase-mimetic activity of Ce^{4+} species in the incorporated CeO_2 nanoparticles, the microrobots showed strong ROS-scavenging ability and could effectively protect cells from oxidative stress-induced damage. In addition, the incorporation of CeO_2 significantly enhanced osteogenic differentiation and extracellular matrix mineralization. The microrobots also degraded gradually through surface erosion within 30 days under physiological conditions.

Collectively, this work presents a biodegradable magnetic microrobot platform that integrates magnetically controlled navigation, antioxidant cytoprotection, and osteogenic mineralization, offering a promising strategy for minimally invasive active bone repair with great potential for clinical translation. A limitation of this study is that the direct magneto-mechanical effect on osteogenesis was not evaluated. Future studies will combine oscillating or rotating magnetic fields with CeO_2-mediated bioactivity to investigate whether magnetic actuation can further promote osteogenesis through mechanical cues, and will focus on *in vivo* bone repair efficacy and long-term biosafety before any clinical translation is considered.

Data availability statement

The authors confirm that the supplementary data are available within this article. The supplementary data mainly comprise the full XPS survey spectrum and the degradation data of the microrobots.

Declaration of generative AI and AI-assisted technologies

During the preparation of Section 2 (Methods), the first author used DeepSeek for language polishing and improving the clarity and readability of the text. The authors reviewed and edited the output and take full responsibility for the content of the manuscript.

Acknowledgments

This work is supported by the National Natural Science Foundation of China (52302343) and Beijing Nova Program (20240484527).

Authors' contribution

Conceptualization, J.L.; methodology, D.S. and Y.Y.; validation, D.S. and Y.Y.; formal analysis, D.S. and Y.Y.; investigation, D.S. and Y.Y.; writing—original draft, D.S.; writing—review and editing, J.L.; supervision, J.L.; funding acquisition, J.L. All authors have read and agreed to the published version of the manuscript.

Conflicts of interest

The authors declare that they have no known competing financial interests or personal relationships that could have appeared to influence the work reported in this paper.

References

[1] Yang J, Chen Z, Gao C, Liu J, Liu K, *et al.* A mechanical-assisted post-bioprinting strategy for challenging bone defects repair. *Nat. Commun.* 2024, 15(1):3565.

[2] Zhou J, Zhang Z, Joseph J, Zhang X, Ferdows BE, *et al.* Biomaterials and nanomedicine for bone regeneration: progress and future prospects. *Exploration* 2021, 1(2):20210011.

[3] Wang X, Zhang D, Peng H, Yang J, Li Y, *et al.* Optimize the pore size-pore distribution-pore geometry-porosity of 3D-printed porous tantalum to obtain optimal critical bone defect repair capability. *Biomater. Adv.* 2023, 154:213638.

[4] Shen J, He R, He J, Liao L, Huang Y, *et al.* Oscillating magnetic field induced bone injury repair by using drug-free micromotors. *Adv. Sci.* 2025, 12(36):e03254.

[5] Zheng Y, Hong X, Wang J, Feng L, Fan T, *et al.* 2D Nanomaterials for tissue engineering and regenerative nanomedicines: recent advances and future challenges. *Adv. Healthc. Mater.* 2021, 10(7):2001743.

[6] Hajiali H, Ouyang L, Llopis-Hernandez V, Dobre O, Rose FRAJ. Review of emerging nanotechnology in bone regeneration: progress, challenges, and perspectives. *Nanoscale* 2021, 13(23):10266–10280.

[7] Szwed-Georgiou A, Płociński P, Kupikowska-Stobba B, Urbaniak MM, Rusek-Wala P, *et al.* Bioactive materials for bone regeneration: biomolecules and delivery systems. *ACS Biomater. Sci. Eng.* 2023, 9(9):5222–5254.

[8] Wei H, Cui J, Lin K, Xie J, Wang X. Recent advances in smart stimuli-responsive biomaterials for bone therapeutics and regeneration. *Bone Res.* 2022, 10(1):17.

[9] Li S, Zhou H, Shi D, Sofer Z, Li J. Micro/nanorobots for detecting and eliminating biological and chemical warfare agents. *BMEMat* 2026, 4(1):e70021.

[10] Xu Y, Zhao J, Xu X, Liu Y, Li Y, *et al.* Engineered biomimetic nanorobots orchestrate targeted nose-to-brain delivery to resolve neuron-glia entanglement against Parkinson's disease. *Small* 2026, 22(18):e13394.

[11] Zhang Z, Wang L, Jiang F, Yu S, Ji F, *et al.* Fully integrated wearable control system for micro/nanorobot navigation. *Int. J. Extrem. Manuf.* 2025, 7(3):035505.

[12] Shi D, Wang X, Deng Y, Zhou H, Wang Y, *et al.* Smart micro/nanorobots for drug delivery in the brain. *Prog. Mater. Sci.* 2026, 155:101533.

[13] Li S, Li J, Shi D, Sofer Z, Zhou H. Magnetically driven BiOI/MnFe2O4 micro/nanorobots for capture, aggregation, and on-site decontamination of biological warfare agents. *Sep. Purif. Technol.* 2026, 380(2):135351.

[14] Urso M, Ussia M, Pumera M. Smart micro- and nanorobots for water purification. *Nat. Rev. Bioeng.* 2023, 1(4):236–251.

[15] Hou J, Liu H, Huang L, Wu SB, Zhang ZL. Recent advances in micro/nano-robots for environmental pollutant removal: mechanism, application, and prospect. *Chem. Eng. J.* 2024, 498:155135.

[16] Kim J, Mayorga-Burrezo P, Song SJ, Mayorga-Martinez CC, Medina-Sánchez M, *et al.* Advanced materials for micro/nanorobotics. *Chem. Soc. Rev.* 2024, 53(18):9190–9253.
[17] Neettiyath A, Pumera M. Micro/nanorobots for advanced light-based biosensing and imaging. *Adv. Funct. Mater.* 2025, 35(8):2415875.
[18] Kim H, Jo K, Choi H, Hahn SK. Biocompatible polymer-based micro/nanorobots for theranostic translational applications. *J. Controlled Release* 2024, 374:606–626.
[19] York PA, Peña R, Kent D, Wood RJ. Microrobotic laser steering for minimally invasive surgery. *Sci. Robot.* 2021, 6(50):eabd5476.
[20] Kim Y, Parada GA, Liu S, Zhao X. Ferromagnetic soft continuum robots. *Sci. Robot.* 2019, 4(3):eaax7329.
[21] Xu C, Jiang Y, Wang H, Zhang Y, Ye Y, *et al.* Arthritic microenvironment actuated nanomotors for active rheumatoid arthritis therapy. *Adv. Sci.* 2023, 10(4):2204881.
[22] Wang B, Chen Y, Ye Z, Yu H, Chan KF, *et al.* Low-friction soft robots for targeted bacterial infection treatment in gastrointestinal tract. *Cyborg Bionic Syst.* 2024, 5:0138.
[23] Mao L, Yang P, Tian C, Shen X, Wang F, *et al.* Magnetic steering continuum robot for transluminal procedures with programmable shape and functionalities. *Nat. Commun.* 2024, 15:3759.
[24] Zhou H, Mayorga-Martinez CC, Pané S, Zhang L, Pumera M. Magnetically driven micro and nanorobots. *Chem. Rev.* 2021, 121(8):4999–5041.
[25] Li C, Zhang W, Chen X, Ding S, Wang L, *et al.* $CD5^+$ dendritic cell robots mediated *in situ* immunocyte activation. *Sci. Adv.* 2026, 12(33):eaee5305.
[26] Li C, Li J, Liu X, Chen X, Ding S, *et al.* Programmable multifunctional microrobots for synergistic cuproptosis-immunotherapy. *Natl. Sci. Rev.* 2026:nwag491.
[27] Chen Y, Du X, Law J, Sun Y. Magnetic micro/nano robots for physical cell stimulation: fundamentals, fabrication, and applications. *Int. J. Extrem. Manuf.* 2026, 8(2):022006.
[28] Chen J, Wang C, Jia L, Zhang T, Li Y, *et al.* Magnetically controlled chlorella-based microrobots loaded with quercetin for precision treatment of anteromedial osteoarthritis. *Adv. Funct. Mater.* 2026, 36(72):2418197.
[29] Ding Z, Cai Y, Sun H, Rong X, Ye S, *et al.* Janus hydrogel microrobots with bioactive ions for the regeneration of tendon-bone interface. *Nat. Commun.* 2025, 16(1):2189.
[30] Tian Y, Han W, Yeung KL. Magnetic microsphere scaffold-based soft microbots for targeted mesenchymal stem cell delivery. *Small* 2023, 19(32):2300430.
[31] Go G, Jeong SG, Yoo A, Han J, Kang B, *et al.* Human adipose–derived mesenchymal stem cell–based medical microrobot system for knee cartilage regeneration *in vivo*. *Sci. Robot.* 2020, 5(38):eaay6626.
[32] Huang H, Li J, Wang C, Xing L, Cao H, *et al.* Using decellularized magnetic microrobots to deliver functional cells for cartilage regeneration. *Small* 2024, 20(11):2304088.
[33] Yang L, He X, Li W, Shang L. Bioinspired magnetic janus core–shell micromotors for delivery of stem cells and vascular endothelial growth factor in bone regeneration. *Adv. Healthc. Mater.* 2026, 15(3):e01294.
[34] Zhang L, Wang S, Hou Y. Magnetic micro/nanorobots in cancer theranostics: from designed fabrication to diverse applications. *ACS Nano* 2025, 19(8):7444–7481.
[35] Ju X, Chen C, Oral CM, Sevim S, Golestanian R, *et al.* Technology roadmap of micro/nanorobots. *ACS Nano* 2025, 19(27):24174–24334.

[36] Reddy LH, Arias JL, Nicolas J, Couvreur P. Magnetic nanoparticles: design and characterization, toxicity and biocompatibility, pharmaceutical and biomedical applications. *Chem. Rev.* 2012, 112(11):5818–5878.

[37] Zhao Y, Xiong H, Li Y, Gao W, Hua C, *et al.* Magnetically actuated reactive oxygen species scavenging nano-robots for targeted treatment. *Adv. Intell. Syst.* 2022;4(7):2200061.

[38] Zhang M, Zhai X, Ma T, Huang Y, Jin M, *et al.* Sequential therapy for bone regeneration by cerium oxide-reinforced 3D-printed bioactive glass scaffolds. *ACS Nano* 2023, 17(5):4433–4444.

[39] Li H, Xia P, Pan S, Qi Z, Fu C, *et al.* The advances of ceria nanoparticles for biomedical applications in orthopaedics. *Int. J. Nanomedicine* 2020, 15:7199–7214.

[40] Li J, Wen J, Li B, Li W, Qiao W, *et al.* Valence state manipulation of cerium oxide nanoparticles on a titanium surface for modulating cell fate and bone formation. *Adv. Sci.* 2018, 5(2):1700678.

[41] Li F, Li J, Song X, Sun T, Mi L, *et al.* Alginate/gelatin hydrogel scaffold containing nCeO2 as a potential osteogenic nanomaterial for bone tissue engineering. *Int. J. Nanomedicine* 2022, 17:6561–6578.

[42] Nag S, Mitra O, Bhattacharjee A, Mohanto S, Gowda BHJ, *et al.* Exploring the emerging trends in the synthesis and theranostic paradigms of cerium oxide nanoparticles (CeONPs): a comprehensive review. *Mater. Today Chem.* 2024, 35:101894.

[43] Ren S, Zhou Y, Zheng K, Xu X, Yang J, *et al.* Cerium oxide nanoparticles loaded nanofibrous membranes promote bone regeneration for periodontal tissue engineering. *Bioact. Mater.* 2022, 7:242–253.

[44] Lu B, Zhu D, Yin J, Xu H, Zhang C, *et al.* Incorporation of cerium oxide in hollow mesoporous bioglass scaffolds for enhanced bone regeneration by activating the ERK signaling pathway. *Biofabrication* 2019, 11(2):025012.

[45] Wang R, He X, Bai J, Su S, Zhou R, *et al.* Cerium oxide nanoparticles-reinforced GelMA hydrogel loading bone marrow stem cells with osteogenic and inflammatory regulatory capacity for bone defect repair. *ACS Appl. Mater. Interfaces* 2024, 16(49):67373–67384.